Chemical pressure in functional materials

Tutorial reviews

Chemical pressure for synthesis of functional materials

Kun Lin[a], Qiang Li[a], Runze Yu[a], Jun Chen[a], and J. Paul Attfield[b,*], Xianran Xing[a,*]

Chemical pressure, a strange but familiar concept, is a lattice internal force caused by chemical modifications and arouses great interest due to its diversity and efficiency to synthesize new compounds and tune functional materials. Different from physical pressure loaded by external force that is positive, chemical pressure can be either positive or negative (contract a lattice or expand it), often through flexible and mild chemical synthesis strategies, which are particularly important as a degree of freedom to manipulate material behaviors. In this tutorial review, we summarize the features of chemical pressure as a methodology and demonstrate its role in synthesizing and discovering some typical magnetic, electric, and thermal responsive functional materials. The measure of chemical pressure using experimental lattice strain and elastic modulus was proposed, which can be used for quantitative descriptions of the correlation between lattice distortion and property. From a lattice strain point of view, we classify chemical pressure into different categories: (i) chemical substitution, (ii) chemical intercalation/de-intercalation, (iii) size effect, and (iv) interface constraint, etc. Chemical pressure, combining chemical bonding, lattice symmetry, local structure, electron structure and phonon structure effects etc., is a general and effective method for synthesizing new compounds and tuning functional materials.

1. The nature of chemical pressure and its features in comparison with physical pressure.
2. Experimental ways to measure chemical pressure.
3. Diverse routes to achieve chemical pressure: (i) chemical substitution, (ii) chemical intercalation/de-intercalation, (iii) size effect, (iv) interface constraint, etc.
4. The role of chemical pressure in modulating magnetic, electric, and thermal responsive functional materials.
5. Current challenges and perspectives of the chemical pressure method for achieving high-performance functional materials.

Introduction

Although unfamiliar to many people, the terminology of "chemical pressure" emerged as a physical quantify nearly one hundred years ago. The story can be traced back to the early twentieth century when the volume of an atom was found to be compressive. T. W. Richards *et al.* claimed that there must be a "intrinsic distending pressure", i.e., chemical pressure, to resist external pressure and chemical affinity in matter:

$$p + \prod = \prod_p + P_\theta \qquad (1)$$

where p presents external physical pressure, $\prod$ presents chemical affinity, $\prod_p$ presents intrinsic distending or repulsive pressure (chemical pressure), and P_θ present thermal pressure— the force of lattice strain induced by thermal expansion.[1, 2] That is, chemical pressure is a passive interatomic force exerted to balance the internal and external forces in solids. One of the most useful feature of chemical pressure is

that it can be modified by elemental substitutions, which facilely controls atomic distance in solids like physical pressure does.[3, 4] Studies to correlate chemical pressure with physical pressure have been carried out, e.g. Nowik *et al.* reported that the valence-phase-transition temperature (T_v) in $Yb_{0.4}1n_{0.6}Cu_2$ intermetallic compound decreases with both physical pressure (hydrostatic pressure) and chemical pressure (via substitution of Yb^{3+} with La^{3+}).[3] The "chemical pressure" concept became popular for explaining variations in the critical temperature of superconductor families such as the copper oxides first discovered in the 1980's and the iron-based superconductors in the 2000's.[5-7] Since then, chemical pressure has been widely used as a counterpoint strategy to physical pressure in the design and synthesis of solids, notably magnetic, electric, and thermal responsive functional materials where properties are very sensitive to lattice strain.

The key point of chemical pressure method is the generation of lattice strain, which is realized by a chemical way instead of a physical one. It changes transitions such as the spin, orbital, and charge orderings of atoms in the lattice, and thus has important influence on material properties. The scope of the chemical pressure method has grown with the chemistry diversity of manipulating the lattice in solids. The employment of chemical pressure has been increasing recognized as a diverse and effective strategy to control material structures at multiple

a) Beijing Advanced Innovation Center for Materials Genome Engineering, Institute of Solid State Chemistry, University of Science and Technology Beijing, Beijing, 100083, China. Email: xing@ustb.edu.cn
b) Centre for Science at Extreme Conditions and School of Chemistry, University of Edinburgh, Edinburgh EH9 3FD, United Kingdom. j.p.attfield@ed.ac.uk

levels and hence to tailor the performances. In this tutorial review, we discussed the nature of chemical pressure and its features in comparison with physical pressure, and we redefine it as a lattice internal force caused by chemical modifications. Chemical pressure can be introduced by the following four chemical routes: (i) elemental substitution[8-12], (ii) small molecules intercalation/de-intercalation[13-16], (iii) size effect[17-21], and (iv) chemical interfaces[22-26]. An experimental method to quantify chemical pressure is proposed. Furthermore, the critical role of chemical pressure in modulating materials properties are exampled in a series of magnetic, electric, and thermal responsive functional materials. Finally, we summarized the current challenges and perspectives of chemical pressure method.
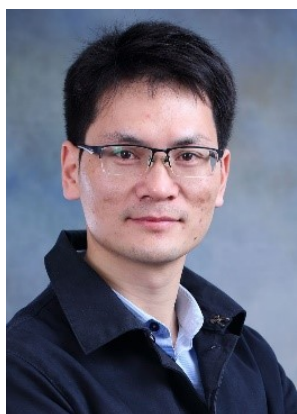
Kun Lin is a professor at Institute of Solid State Chemistry, University of Science and Technology Beijing, China (USTB). He received his BS in Metallurgical Engineering from Northeastern University, China, in 2011, and PhD in Metallurgical Physical Chemistry from USTB in 2017 under the supervision of prof. Xianran Xing. His current research interest includes the design and synthesis of high-performance rare-earth-based metallic materials that exhibit controllable thermal expansions and related properties, and to elucidate the interplay among the structure, magnetism, transport, and mechanical properties.

Kun Lin

Qiang Li received his BS and Ph.D from the Department of Physical Chemistry at USTB in 2012 and 2019. Now he jointed Prof. Xianran Xing's group as the associate professor of Institute of Solid State Chemistry, USTB. In recent years, he has focused on local structural issues (PDF, XSAFS, RMC, TEM etc.) in catalysis, negative thermal expansion, and functional design for solid-state chemistry.

Qiang Li

Runze Yu received his BS in Solid State Physics from Jilin University in 2005, and obtained his PhD in Condensed Matter Physics from Institute of Physics, Chinese Academy of Sciences (IOP, CAS) in 2012. After three years post-doc at Tokyo Institute of Technology and one and half year post-doc at Brookhaven National Laboratory, he started his work at IOP, CAS from 2017 as an associated professor. He became a full professor of Institute of Solid State Chemistry, USTB from 2021. His current research includes synthesis and characterization of novel functional and quantum materials using high pressure technique; exploration of emergent quantum materials and phenomena under high-pressure extreme conditions.

Runze Yu

Jun Chen is currently a full professor at USTB. He earned his PhD in Metallurgical Physical Chemistry from USTB, China, in 2007. In 2008–2009, he was financially supported by the Alexander von Humboldt Fellowship at TU-Darmstadt, Germany. In 2015, he worked in Materials and Structures Laboratory, Tokyo Institute of Technology, Japan, as an oversea guest professor. In 2019, he worked in Department of Physics and Astronomy, University of Padova, Italy, as a visiting scientist. Dr. Chen's current research includes crystal structure, correlations with physical or chemical properties, and new materials design for ferroelectrics, piezoelectrics, magnetics, and negative thermal expansion solids.

Jun Chen

J. Paul Attfield holds a Chair in Materials Science at Extreme Conditions at the School of Chemistry and Centre for Science at Extreme Conditions, University of Edinburgh. He received B.A. and D.Phil. degrees from Oxford University, and he was a Co-Director of the Interdisciplinary Research Centre in Superconductivity at the University of Cambridge during 1991-2003. He received the Royal Society of Chemistry's Meldola and Corday-Morgan medals and Peter Day award, and

J. Paul Attfield

he was elected a Fellow of the Royal Society in 2014. Early research contributions included pioneering resonant X-ray scattering experiments of cation and valence ordering, and studies of disorder effects in functional oxides. Current research is centred on electronic and magnetic materials including use of high-pressure methods.

Xianran Xing

Xianran Xing is a Changjiang professor at USTB, and head of Institute of Solid State Chemistry, USTB. He received his BS degree in Chemistry from Anqing Normal University in 1988, and his PhD in Physical Chemistry from USTB in 1994. He became a fellow of Royal Society of Chemistry (FRSC) in 2014. Over the last 20 years, he has led a group to perform pioneering work in the development of negative thermal expansion (NTE) in perovskite compounds, correlated with ferroelectric, magnetoelectric and multiferroic properties. His research interests focus on solid state chemistry, including synthesis strategies, local structure with PDF technique and RMC method, crystal structures and chemical pressure design for obtaining functional materials.

Chemical pressure versus physical pressure

It is intuitive that applying a high physical pressure on a solid can change its lattice through compressibility, which alters the chemistry of an atom by activating its inner electrons and unoccupied orbitals, leading to many new and surprising phenomena[27, 28]. Alternatively, the lattice can be changed by a chemical route at ambient pressure, i.e., by chemical pressure. The critical role of physical pressure in synthesizing new compounds and revealing new physics in solids is evident; nevertheless, high pressure synthesis and characterizations are generally complex and expensive[27, 29]. Besides, some solid materials, based on radioactive actinides for instance, are not convenient for characterization under physical pressure[30]. By comparison, chemical pressure is a gentle and convenient way to change the size of a lattice, which facilitates both material synthesis and property characterizations.

The importance of chemical pressure can be well exampled in the studies of 1111-type LnFeAsO-based superconductors (Ln = Rare earths). LnFeAsO-based compounds generally adopt tetragonal $P4/nmm$ symmetry, constituted by edge-sharing $FeAs_4$ and $(O,F)Ln_4$ tetrahedra layers stacking alternatively along the [001] axis (Fig. 1a). Hosono *et al.* discovered the appearance of superconductivity in $LaFeAs(O_{1-x}F_x)$ (x = 0.05-0.12) with T_c of 26 K.[31] Immediately, it was found that increasing the pressure enables a rapid increase in the T_c of $LaFeAs(O_{1-x}F_x)$. The onset T_c reaches a maximum of 43 K, well above the McMillan limit,[32] at 4 GPa and then decreases with further increasing pressure.[33] Interestingly, the emergent high-temperature

superconductivity can be realized by chemical pressure method at ambient pressure. Replacing La^{3+} with smaller rare earth cations in $LnFeAs(O_{1-x}F_x)$ ($x \approx 0.10$), the T_c increases from 26 K for La^{3+} to 41 K for Ce^{3+}, to 52 K for Pr^{3+}, and to a maximum of 55 K for Sm^{3+},[34] which further decreases to 51 K for Tb^{3+}, to 41 K for Dy^{3+}, and to 33 K for Ho^{3+}.[35] Therefore, as shown in Fig. 1b-1c, chemical pressure and physical pressure have rather similar superconducting phase diagrams for the LnFeAsO-based compounds. Fig. 1c shows the pnictogen height (the distance of the As to the Fe plane in the FeAs layers) dependence of T_c for the typical Fe-based superconductors. There exists a generally symmetric curve with a peak around a critical pnictogen height of 1.38 Å that is in favor of superconducting state.[36, 37] The universal mechanism for both physical pressure and chemical pressure can be understood by the regulation of pnictogen height in Fe-based superconductors. This also illustrates the more general point that chemical pressure effects in complex materials can be positive or negative. This arises when some structural geometry is optimum for the property of interest (represented by the pnictogen height in the $LnFeAs(O_{1-x}F_x)$ series). Starting from the largest Ln = La, increasing chemical pressure (decreasing Ln^{3+} radius) initially increases T_c until geometry is optimum for Ln = Sm, but then decreases it for the smaller Ln cations as shown in Fig. 1c. Another example of optimal structure geometry is in perovskites with tolerance factor t =1 as described later in the *Chemical Substitution* section. The first superconductor with T_c higher than the boiling point of liquid nitrogen, $YBa_2Cu_3O_7$, was also designed by a chemical pressure method (replacing La^{3+} in $La_{2-x}Ba_xCuO_4$ with Y^{3+}) although this led to an unexpected change in structure type.[7, 34]
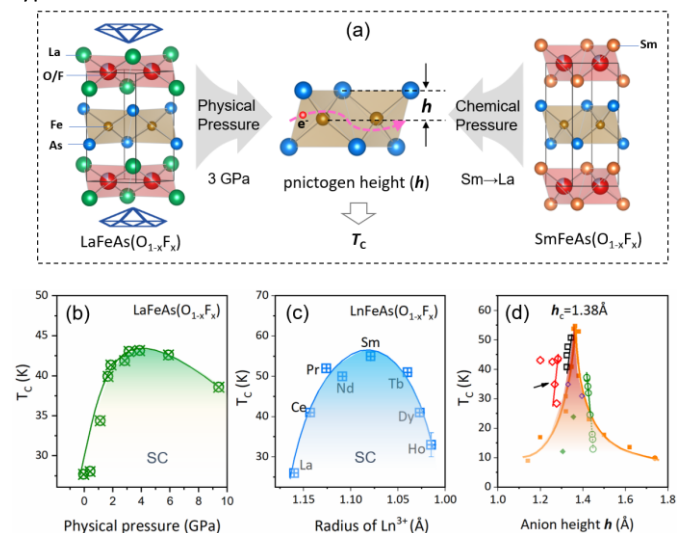
Fig. 1 (a) Crystal structure of LnFeAsO-based compounds (Ln = rare earths) modified by physical (left) and chemical (right) pressure, respectively. Both physical pressure and chemical pressure controls the pnictogen height of the FeAs layer which determines the superconductivity transition temperature (T_c) via regulation of electronic structure. (b,c) experimental phase diagrams of the $LaFeAs(O_{1-x}F_x)$ system by physical (b) and $LnFeAs(O_{1-x}F_x)$ by chemical pressure (c). There is a good similarity between the superconductivity phase diagrams of physical and chemical pressure. (d) pnictogen height (h) dependence of T_c for the typical Fe-based superconductors. A peak at ~1.38 Å corresponds to the highest T_c for both physical and chemical pressure. Filled symbols represent the data at ambient pressure and

open symbols are the data under the optimal pressure. Details are shown in Ref. ([37]). Red diamonds (marked by arrow) indicate physical pressure on LaFeAs(O$_{1-x}$F$_x$).

Physical pressure changes the lattice in solids without introducing other variables. However, chemical pressure usually brings new variables to the parent material, such as new atoms, molecules, or interfaces. These new variables alter the structure of the host lattice at multiple levels, and can modify material properties as well. To isolate the "pressure" effect of chemical pressure, elements with similar chemical properties but different sizes, i.e., possessing the same charges and similar electronic structures, are ideal. Common examples are lanthanide (rare earth) Ln^{3+} cations and M^{2+} alkaline earth (M = Ca, Sr, Ba) cations, as illustrated in studies of chemical pressure effects on LnFeAs(O$_{1-x}$F$_x$) superconductors above and thermoelectric performance in LnSb$_2$O$_2$ (Ln = La, Nd, Sm, Gd, Ho, and Er),[11] and on phonon vibration in Ba$_{1-x}$Sr$_x$FCl (0 ≤ x ≤ 3)[38].
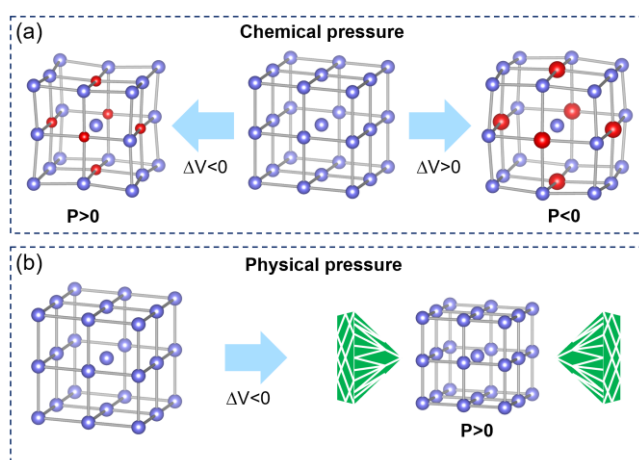

Fig. 2 Schematic of chemical pressure (a) versus physical pressure (b).

A great advantage of chemical pressure is that both positive pressure and negative pressure can be realized.[18, 21, 39-41] Physical pressure presses a material down and diminishes its volume, which is usually defined as positive pressure. By contrast, chemical pressure can either diminish the volume or expand it, see Fig. 2.[42-44] The latter is usually defined as negative (chemical) pressure. Negative pressure provides an important degree of freedom for materials design in solids, making it a powerful method to synthesize new solids and to discover unusual properties.[18, 21, 40, 41] In freestanding PbTiO$_3$ nanowires, for example, negative pressure produces a lower-density "PX" phase to a higher-density perovskite phase transformation, which enhances the tetragonality, Curie temperature and spontaneous polarization.[18] In CuO and MnF$_2$ nanoparticles, the negative pressure induced by size effect greatly prompts the magneto-lattice effect and transforms the thermal expansion behavior from positive to negative below the magnetic ordering temperature.[17]
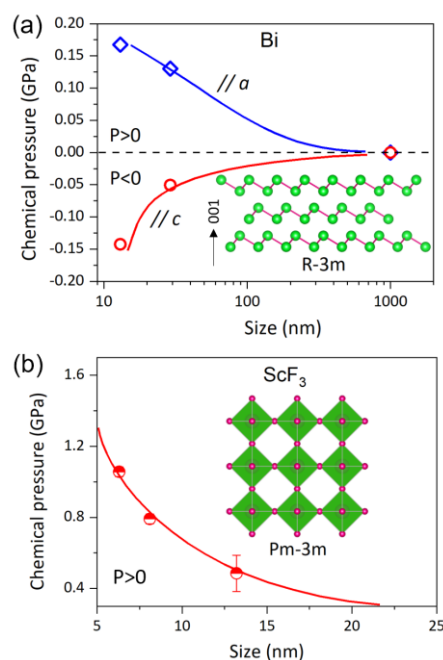
Fig. 3 Anisotropic and isotropic chemical pressure in rhombohedral Bi (a) and cubic ScF$_3$ (b) in nanoparticles, respectively.

Due to structural anisotropy, chemical pressure can possess different signs along different directions, i.e., it can be negative along one crystallographic direction while being positive along another. Semimetal bismuth has the rhombohedral A7-type structure built up by corrugated layers parallel to the (111) planes.[19] Inside the plane, each atom is bonded to three nearest-neighbor atoms at 3.072 Å by a so-called metal-metal covalent bond, while the shortest distance between the atoms in adjacent layers is 3.529 Å. This gives rise to strong anisotropy in Young's modulus of 21 GPa and 31 GPa respectively along the a and c axis[45]. When the particle size reduces to the nanoscale, size effect-induced chemical pressure are strongly anisotropic.[19] When average particles sizes reduced to 28.5nm and 13.1 nm, the a axis contracts by 0.42% and 0.54%, corresponding to positive chemical pressure of 0.13 GPa and 0.17 GPa; while the c axis expands by 0.24% and 0.67%, corresponding to negative chemical pressure of -0.05 GPa and -0.14 GPa (Fig. 3a). The anisotropic chemical pressure increases the bond angle that relaxes under the thermal activation with rising temperature, and induces a transition of coefficient of thermal expansion from positive to negative along the c axis in nanosized bismuth.[19] By compassion, the size effect-induced chemical pressure in cubic ScF$_3$ has the same sign (P>0 here) due to its isotropic character (Fig. 3b)[46].

Measure of chemical pressure

Although widely used, chemical pressure has not been truly measured and quantified by experiments so far[21, 41, 47-49]. Physical pressure is external and can be quantified by direct or indirect measurement of force/area, while chemical pressure is internal and cannot be measured directly. Instead, the degree of lattice strain was often used to describe chemical pressure in

solids, such as 2% compressive strain of chemical pressure[12, 26, 41, 49]. However, using lattice strain to evaluate chemical pressure is indirect and inadequate. This is because the comparison of chemical pressures by a lattice strain method is limited to the specific materials in a study, as different materials types differ greatly in compressibility or elastic modulus[1]. We can assert that a 2% lattice strain in $Ba_{1-x}Sr_xTiO_3$ by Sr^{2+} substitution for Ba^{2+} produces a larger chemical pressure than a 1% strain does, but we cannot simply assert that a 2% strain in $Fe_{1-x}Ni_x$ produces a larger chemical pressure than a 1% strain in $Ba_{1-x}Sr_xTiO_3$. Furthermore, chemical pressure should have the same force/area units as external pressure (Pa, bar, torr, etc.). So, how to quantify the chemical pressure?

Fredrickson *et al.* have developed a density functional theory-chemical pressure (DFT-CP) analysis based on electronic interaction in intermetallic compounds[50, 51]:

$$P = -\frac{\partial E}{\partial V} = -\sum_i \sum_j \frac{\partial}{\partial V}\left(\gamma H_{ij}^2 + \left(\sum_n o_n c_{n,i}^* c_{n,j}\right) H_{ij}\right) = \frac{1}{N_{orb}}\sum_i \sum_j p_{ij} \quad (2)$$

where E is the total energy expressed as a sum of onsite and pairwise interaction terms[52], V is cell volume, H_{ij} is the Hamiltonian matrix elements of (H_{ij}), o_n is the occupancy of that crystal orbital, $c_{n,j}$ is the coefficient of atomic orbital j in crystal orbital n, N_{orb} is the number of orbitals in the crystal, and p_{ij} is the pressure arising from the interaction between atomic orbitals i and j ($i = j$ terms are zero). The DFT-CP method can be employed to calculate and interpret the chemical pressure distributions inside the crystal structures based on DFT results.[9, 50, 51, 53] For example, they calculated the μ_2-Huckel chemical pressure of $SrAg_5$ and a hypothetical $CaAg_5$ phase (Fig. 4). The Sr atom has a net negative chemical pressure of -8.2 GPa, which is balanced by the positive chemical pressure values of the Ag atoms of 1.7 GPa. Replacing Sr with the smaller Ca, the net chemical pressure at the Ca atom increases to -10.2 GPa; such a strong chemical pressure drives a transition to the Ca_2Ag_7 structure with chemical pressure reduced to -1.2 GPa. The DFT-CP method is a useful tool to calculate the chemical pressure at atomic level, and provides visual prediction of the structural stability and phase transformation.
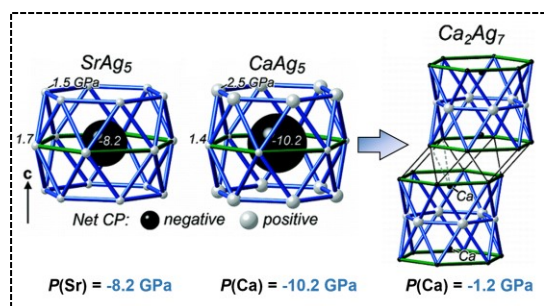
Fig. 4 Left: DFT-CP analysis of the chemical pressure in $CaCu_5$-type $SrAg_5$ phase and hypothetic $CaAg_5$ phase. Net chemical pressure values for the Sr or Ca atom and their neighboring Ag atoms are plotted as spheres. Right: the structural phase transition from $CaCu_5$-type $CaAg_5$ phase to Ca_2Ag_7 phase to relax the strong local chemical pressure. The balls: black for negative, white for positive, radius giving the magnitude

Besides the above theoretical analysis, here we propose two experimental ways to quantify chemical pressure in solids. The

first one is to apply both physical pressure and chemical pressure to a material; the magnitude of chemical pressure should equal to that of physical pressure that (if it can) causes the same lattice strain (or volume change, in the parent material), see Fig. 5. In other words, if the chemical pressure and the physical pressure generate the same lattice (or volume) change in a material, we propose that they are equivalent in magnitude. This idea is analogue to an ancient Chinese idiom story "Cao Chong weighs an elephant": the mass of an elephant is determined by weighing many stones that generate the same draught (water-displacement) of a boat, instead of weighing the elephant itself.
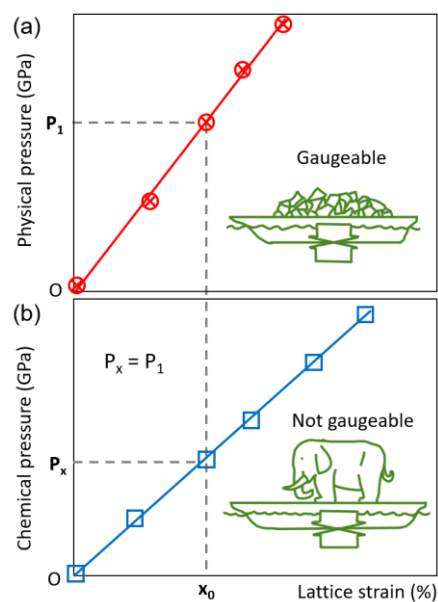
Fig. 5 A schematic presentation of the way to quantify chemical pressure in solids. The magnitude of chemical pressure (b) equals to the magnitude of physical pressure (a) that causes the same lattice strain. Inset describes an ancient Chinese idiom story "Cao Chong weighs an elephant" in ~200 A.D.: the mass of an elephant is determined by weighing stones that generate the same draught on a boat, because the elephant itself was too large to weigh at that time.

The second experiment method introduced below is more convenient and straightforward and so we highly recommend it. In material science, the relationship between strain and stress in a material follows the Hooke's law during elastic deformation $\sigma = E\,e$, where σ is the stress, e is the strain along loading direction, and E is the Young's modulus. Since the nature of chemical pressure can also be considered as elastic lattice strain, in a chemical way instead of a physical one, we can describe chemical pressure by applying Eq. (1-2):[54]

$$dP = -E\frac{dx}{x_0} \quad (3)$$

where dP is chemical pressure, dx is the change in lattice size (by chemical pressure), x_0 is initial lattice size, and E is Young's modulus. All parameters, dx, x_0 and E, are measurable (dx and a_0 can be determined by X-ray diffraction, E can be measured by velocity measurement and is known or can be calculated for most compounds). The negative sign defines compressive stress to be positive and tensile stress to be negative, to keep in accordance with physical pressure. Alternatively, we can use the volumetric change to describe chemical pressure by:

$$dP = -K\frac{dV}{V_0} \tag{4}$$

where dV is the change in cell volume, V_0 is initial cell volume, and K is bulk modulus ($K = E/[3(1-2\mu)]$, μ is Poisson's ratio). In fact, Eq. (4) is most often used to describe the compressibility of material under uniform hydrostatic pressure. Note that the modulus of E and K vary with composition, but the change is relatively small when the structure-type and chemical composition do not change much (e.g., K is 97 GPa, 93 GPa and 103 GPa respectively for YFe_2, $TbFe_2$ and $ErFe_2$[55]).

Eq. (3) describes the chemical pressure along a certain direction in solids, which is especially useful for thin films and low symmetry structures where the lattice strain is highly anisotropic. Orientation dependence is unique to chemical pressure. It plays a key role in many remarkable physical properties that are inaccessible by isotropic hydrostatic physical pressure, such as the emergent polar vortices in ferroelectric thin films.[18, 22, 24, 49, 56] Eq. (4) is more suitable for isotropic chemical pressure, like size effect in nanoparticles, and chemical substitution in high symmetry structures. We note that from Eq. (3) and (4), the magnitude of chemical pressure is a relative value. Its value should be based on a given reference state that is defined as the unstrained state. For a given reference state, the chemical pressure is proportional to the rigidity of the structure and the degree of deformation it undergoes. The magnitude of chemical pressure obtained from Eq. (3) and (4) can be used for quantitative comparison among solids in different types. Some examples of chemical pressure values in solids based on experimental lattice strain and elastic modulus are shown in Table 1.

Table 1 Examples of experimental chemical pressures based on Eq. (1-2) and Eq. (1-3)

Compound	Variable	Strain	Bulk modulus B; Young's modulus E	Chemical pressure/GPa	Ref.
$Ce_{1-x}La_xO_{2-y}$	x = 2%	$\Delta V/V_0$ = 0.28%	B = 176.9 GPa[57]	-0.50 GPa	
	x = 5%	$\Delta V/V_0$ = 0.58%		-1.03 GPa	58
	x = 10%	$\Delta V/V_0$ = 0.87%		-1.52 GPa	
$La_{1-x}Sr_xMnO_3$	x from 0.55 to 0.85	$\Delta V/V_0$ = -2.43%	B = 230 GPa[59]	5.58 GPa	60, 61
$FeSe_x$	x from 0.82 to 0.88	$\Delta V/V_0$ = -0.115%	B = 30.7 GPa[62]	0.035 GPa	63
$Tb(Fe_xCo_{1-x})_2$	x = 0.15	$\Delta V/V_0$ = 0.84%	B = 129 GPa[64]	-1.09 GPa	65
VCoNi alloy	Cr replacing V	$\Delta V/V_0$ = -4.305%	B = 72 GPa	3.10 GPa	66, 67
Mg-xAl alloy	x from 0.29% to 2.40%	$\Delta V/V_0$ = -0.73%	B = 35.8 GPa[68]	0.26 GPa	69
Nano CeO_2	18 nm	$\Delta V/V_0$ = -0.23%	B = 177 GPa[57]	0.41 GPa	70
	5 nm	$\Delta V/V_0$ = -0.40%		0.72 GPa	
Nano TiO_2	16 nm	$\Delta V/V_0$ = 0.036%	B = 243 GPa[71]	-0.089 GPa	
	8 nm	$\Delta V/V_0$ = 0.29%		-0.70 GPa	72
	4 nm	$\Delta V/V_0$ = 0.34%		-0.84 GPa	
Nano $PbTiO_3$	36 nm	$\Delta V/V_0$ = 0.4%	B = 141 GPa	-0.56 GPa	21
	12nm	$\Delta V/V_0$ = 2.2%		-3.0 GPa	
Nano Bi (rhombohedra)	13 nm	$\Delta a/a_0$ = -0.54%	E_a = 140 GPa[45]	0.17 GPa	
	29 nm	$\Delta c/c_0$ = 0.67%	E_c = 143 GPa[45]	-0.14 GPa	19
		$\Delta a/a_0$ = -0.42%		0.13 GPa	
		$\Delta c/c_0$ = 0.24%		-0.05 GPa	
$FeSe/SrTiO_3$ thin films	FeSe layers:				
	35	$\Delta a/a_0$ = 0.27%	E_a = 80 GPa[73]	-0.21 GPa	
	25	$\Delta a/a_0$ = 0.80%		-0.64 GPa	74
	1	$\Delta a/a_0$ = 2.65%		-2.12 GPa	
$PbTiO_3$	$PbTiO_3$/PbO epitaxial composite	$\Delta V/V_0$ = 17.1%	B = 141 GPa[75]	-24 GPa	25

Diverse routes for chemical pressure

Chemical substitution The most used chemical pressure method is chemical substitution by introducing different atoms into the lattice. (This is most simply done by using cations of the same valence as noted above, as introduction of aliovalent species can lead to further effects such as electronic doping or vacancy or interstitial formation.) Up to some limit of structural tolerance, an atom in the host lattice can be replaced by a new one of different size. If replaced by a larger one, the lattice expands and vice versa, known as Vegard's law if the lattice

parameters change linearly[76]. The substitution produces a stereochemical interaction at the substitution site and a local strain gradient propagating from it (Fig. 6a). This brings negative or positive pressure to the host lattice, breaks the ideal 3D translational periodicity, and changes the properties in solids.
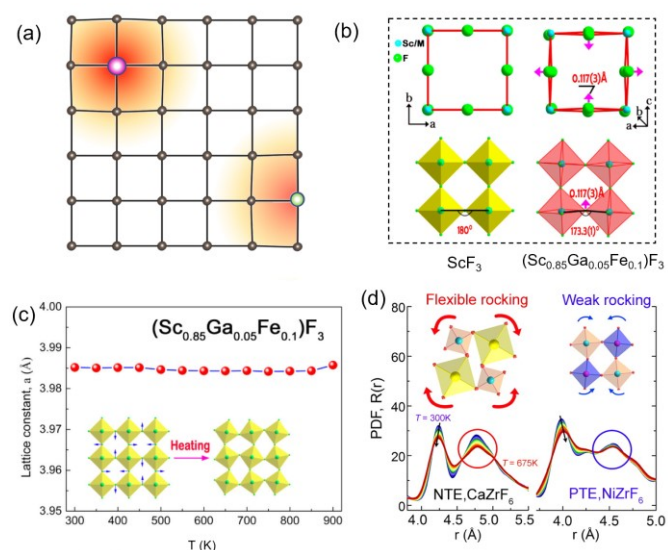
**Fig. 6** (a) Schematic presentation of chemical pressure induced chemical substitution in ReO_3 type metal fluorides. (b) Local structure of ScF_3 (cubic) and $(Sc_{0.85}Ga_{0.05}Fe_{0.1})F_3$ (rhombohedral). (c) Zero thermal expansion in $(Sc_{0.85}Ga_{0.05}Fe_{0.1})F_3$ through positive chemical pressure-driven local structure distortion. Inset shows the rotary coupling of the ScF_6 octahedra rigid units giving rise to zero thermal expansion. (d) Temperature dependence of X-ray PDF radial distribution function, R(r), from room temperature to 675 K for NTE $CaZrF_6$ and $NiZrF_6$. Inset shows two rocking models of $MZrF_6$ substructures.

Negative thermal expansion (NTE) in open-framework structure is driven by low-frequency phonon modes, which is coupled to structural symmetry and can be well-controlled by chemical pressure[77, 78]. For example, ScF_3 has a cubic ReO_3-type structure (Pm-3m) built up by corner sharing ScF_6 octahedra and displays unusual NTE covering a broad temperature range of 10-1100 K[79]. The NTE is correlated to the rotary coupling of the ScF_6 octahedra rigid units with the average Sc-F-Sc angle to be 180° (Fig. 6b)[79, 80], generating phonon modes with negative Grüneisen parameters[46, 81]. Slight chemical substitution by isovalent but smaller cations, i.e., $(Sc_{0.85}Ga_{0.05}Fe_{0.1})F_3$, introduces positive chemical pressure to the structure (Fe^{3+}: 0.645 Å, Ga^{3+}: 0.62 Å, Sc^{3+}: 0.745 Å)[8]. X-ray pair distribution function (PDF) analysis indicates that the symmetry of $(Sc_{0.85}Ga_{0.05}Fe_{0.1})F_3$ transforms to rhombohedral in the short-range (R-3c, r < 20 Å). Such a chemical pressure induced structure distortion changes the Sc-F-Sc bond angle to be 173.3°, which hinders the transverse thermal vibration of fluorine atoms. As a result, the NTE is suppressed to zero thermal expansion (Fig. 6c)[8]. The short-range structure of ScF_3 can be further modulated by chemical pressure method in the $MZrF_6$ series (M = Ca, Mn, Fe, Co, Ni and Zn). It was found that the flexibility of the metal···F atomic linkage driven by size misfit at the M site governs the phonon modes and thus controls the thermal expansion. A flexible metal···F atomic linkage induces NTE for M = Ca, Mn, Fe; while the stiff ones bring positive

thermal expansion (PTE) for M = Ni, Co. Thus, thermal expansion could be tuned from negative, to zero, and to positive by the chemical substitution method (Fig. 6d)[82].
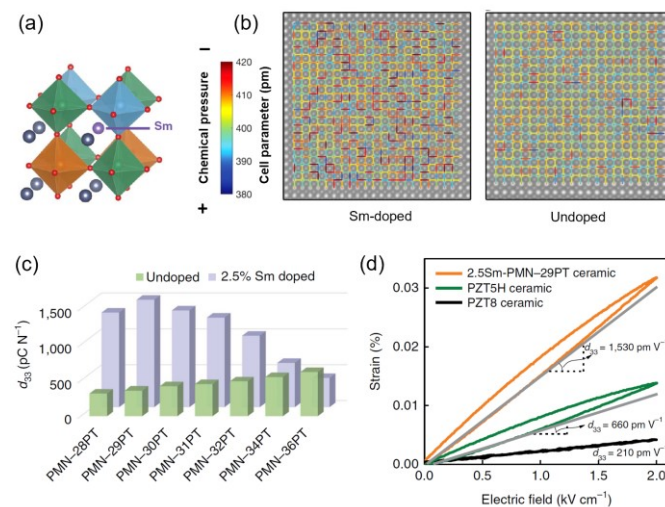
Fig. 7 (a) The crystal structure of Sm-modified $Pb(Zn_{1/3}Nb_{2/3})O_3$–$PbTiO_3$ (PMN–PT) ceramics. (b) Local atomic distances between A-site positions in Sm-PMN-PT (left) and PMN-30PT (right) crystals, revealed by atomic-resolution HAADF-STEM images. The color of the lines represents the distance between A-site atom columns. Larger and shorter distances correspond to negative and positive chemical pressure, respectively. (c) The piezoelectric coefficient d_{33} of 2.5 mol% Sm-modified PMN–xPT and unmodified PMN–xPT ceramics. (d) Electric-field-induced strains of the 2.5Sm-PMN–29PT compared with commercial PZT5H and PZT8 ceramics measured at 1 Hz.

The piezoelectric effect arises from net movement of positive and negative ions with respect to each other under stress, resulting in an electric dipole or polarization. The mobility and flexibility of cations are sensitive to their local coordination environments and are liable to variation by chemical pressure. Li *et al.* conducted chemical substitution using traces of small Sm^{3+} cations (1.24 Å) for Pb^{2+} (1.49 Å) cations in $Pb(Zn_{1/3}Nb_{2/3})O_3$–$PbTiO_3$ (PMN–PT) solid solutions and introduced positive chemical pressure. A combined atomic-lever scanning transmission electron microscopy (STEM) and first-principles calculations demonstrated that the substitution induces significant local structural heterogeneity, which perturbs the local order parameters of polarization, and leads to heterogeneous polar regions and additional interfacial energies[10] (Fig. 7a,7b). As a result, an extraordinarily large piezoelectric constant ($d_{33} > 1,500$ pC N^{-1}) was observed in 2.5 mol% Sm-modified into $0.71Pb(Zn_{1/3}Nb_{2/3})O_3$–$0.29PbTiO_3$ (2.5Sm-71PMN–29PT) ceramic, in large contrast to the undoped counterpart (~500 pC N^{-1})[83] (Fig. 7c,7d). In 1 mol% Sm-modified 70PMN-30PT single crystal, they achieved an even larger piezoelectric constant ($d_{33} > 3400$ pC N^{-1})[10] Similarly, Ranjan *et al.* reported an extraordinarily large electrostrain up to 1.3% in La-doped $0.55Bi_{1-y}La_yFeO_3$–$0.45PbTiO_3$ ($y = 0.3$) solid solution ceramics[84]. Such a large electrostrain behavior is related to the chemical pressure induced structure disorder due to size misfit among Pb^{2+}, Bi^{2+} and La^{3+} cations, which leads to a low-symmetry ferroelectric phase, a large spontaneous lattice strain, domain miniaturization, and an appropriate ferroelectric domain switching[84].

Generally, the extent of chemical substitution has an upper limit. It depends mainly on the size, charge, and electronegativity of the atoms— the more similar the atoms, the higher degree of the substitution. In simple structure types, the range of sizes can be quantified based on geometric relations. This is much studied in the *ABX*$_3$-type perovskite structure where the limit of chemical substitution can be evaluated by the Goldschmidt tolerance factor *t* [85]:

$$t = \frac{r_A + r_X}{\sqrt{2}(r_B + r_X)} \tag{5}$$

where r_A, r_B, and r_X are the average ionic radii of *A*, *B* and *X* site species respectively. For an ideal cubic perovskite structure *t* = 1, indicating that the structure is perfectly matched among *A*, *B* and *X* cations. In Ba*M*O$_3$ (*M* = transition metal) perovskites, for example, the tolerance factor *t* is largely within the range of 0.93–1.05[86]. Transition temperatures for electronic or magnetic orders typically have a maximum value at *t* = 1 and decrease rapidly as *t* falls away from this value.[87] The same is also true in principle for *t* >1, but in practice this often leads to changes in structure to other hexagonal-type perovskites. High (physical) pressure has been used to stabilize some cubic-type Ba*M*O$_3$ perovskites, e.g. cubic-BaRuO$_3$ (*t* = 1.06) has ferromagnetic *T*$_C$ = 60 K whereas SrRuO$_3$ (*t* = 1.02) has *T*$_C$ = 160 K.[88]

Chemical intercalation/de-intercalation. Chemical intercalation (or de-intercalation) reaction introduces (or removes) new chemical entities into (or from) a host lattice, such as molecular water, carbon dioxide, etc. The intercalation (or de-intercalation) of these guests expands (or shrinks) the host lattice and hence induces chemical pressure. This kind of chemical pressure is usually introduced in metal–organic frameworks (MOFs) or other inorganic structures with significant void space[13, 15, 89, 90].

The MOF compound [{Ru$_2$(F$_3$PhCO$_2$)$_4$}$_2$TCNQ(OEt)$_2$] (**1**) crystallizes in a triclinic D$_2$A-layered structure and displays ferromagnetic ordering at ground state (Fig. 8a) (30). Viewing down the *a'* axis, the four CN groups of TCNQ(OEt)$_2$ are coordinated with the [Ru$_2$] units to form a wavy layered two-dimensional network (D$_2$A layer) that lies on the (020) plane with an interlayer distance of 8.07 Å (Fig. 8b). This compound absorbs CO$_2$ into the center of the hexagonal fishnet with an amount of 113 ml STP g^{-1} (10.6 molecules per formula unit) at 99 kPa (**1**⊃CO$_2$). Accordingly, the cell volume increases sharply from 1763.0(2) Å^3 for **1** to 2172.3(3) Å^3 for **1**⊃CO$_2$ by a rate of 23%, and induces significant negative chemical pressure of -3.05 GPa (*B* = 13.3 GPa by our calculations) to the lattice (Fig. 8c). As a result, the TCNQ(OEt)$_2$ and Ru–N – C bending angle reduces accordingly in **1**⊃CO$_2$, flattening the D$_2$A layer and expanding interlayer distance to 8.93 Å (Fig. 8d). Due to the sensitivity of magnetism to the distance between magnetic atoms, this switches the electronic state from a one-electron-transferred state into the neutral state, and transforms the magnetic property from ferrimagnetic to paramagnetic (Fig. 8e-8g). Such a magnetic phase change is reversable by the guest CO$_2$ molecules intercalation/de-intercalation in the framework[16].
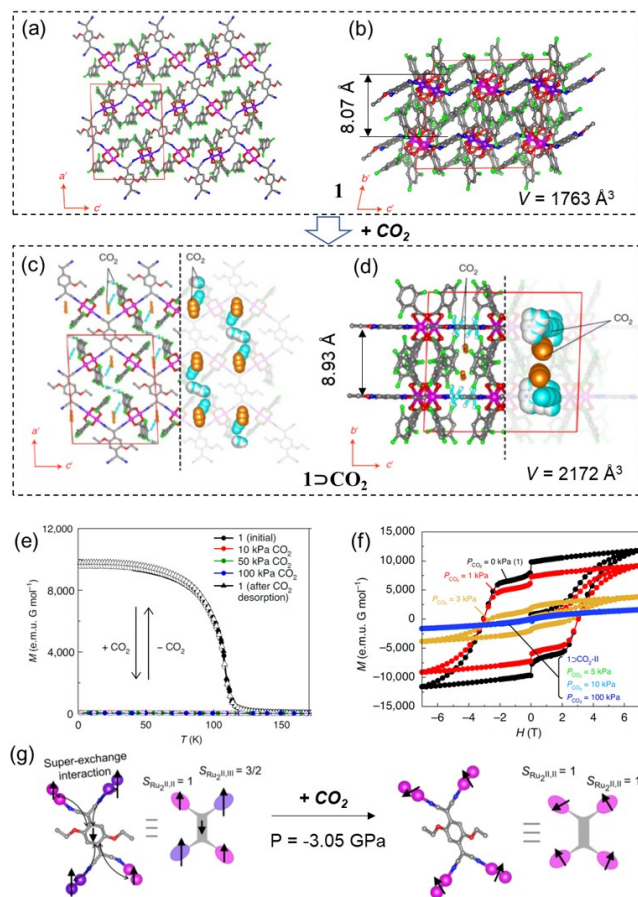
Fig. 8 Chemical pressure induced transitions between paramagnetism and ferrimagnetism in MOF compound [{Ru$_2$(F$_3$PhCO$_2$)$_4$}$_2$TCNQ(OEt)$_2$]. (a, b) Crystal structure of **1** viewing down the *b'* and *a'* directions, respectively. (c, d) Crystal structure of CO$_2$-accommodated phase (**1**⊃CO$_2$) viewing down the *b'* and *a'* directions, respectively. (e) The CO$_2$ pressure dependence of *M–T* curves at 1 kOe during cooling (filled symbols) and heating (open symbols) processes. (f) CO$_2$ pressure dependence of *M–H* curves at 1.8 K. (g) The schematic representations of electronic state in Ru$_2$(F$_3$PhCO$_2$)$_4$ and TCNQ(OEt)$_2$ moieties in **1** (left) and **1**⊃CO$_2$ (right)

In open-framework structures, the NTE originates from transverse thermal vibrations of atoms where the "true" bond lengths are longer than "apparent" bond length, as schemed in Fig. 9a. Such transverse thermal vibrations should be hindered or reduced by additional chemical pressure from guest ions or molecules in the empty space of framework.[14, 77] For YFe(CN)$_6$-based Prussian blue analogues, the NTE is dominated by the transverse motion of N and C atoms. In YFe(CN)$_6$, Fe atoms coordinates to six C atoms to form regular octahedra (FeC$_6$) and Y atoms coordinates to six N atoms to give a bicapped distorted trigonal prism (YN$_6$). The FeC$_6$ and YN$_6$ groups are bridged through CN units in the entire structure with nearly linear Y-N-Fe linkage (176.01(1)°). After intercalation, K$^+$ and H$_2$O are located in the pores near the YN$_6$ trigonal prism of YFe(CN)$_6$, see Fig. 9c,9f. and the cell volume and atomic positions change due to electrostatic interactions. The cell volume of KYFe(CN)$_6$ dramatically contracts by 18.3% compared with that of YFe(CN)$_6$ accompanied by a reduction of Y-N-Fe angle (140.54(5)°). These guest ions or molecules act as barriers to block the transverse thermal vibrations. As shown in Fig. 9d,9e, the transverse vibrational mode of NTE in YFe(CN)$_6$ at 44 cm^{-1} shows the

strongest negative Grüneisen parameter and is the main contribution to NTE. However, for KYFe(CN)$_6$, the low-frequency contribution of N and C atoms is much weakened due to the presence of K$^+$ ions. The lowest energy mode of KYFe(CN)$_6$ at 49.6 cm^{-1} has a small negative value of Grüneisen parameter (Fig. 9g,9h). In this way, the thermal expansion of YFe(CN)$_6$ can be substantially switched from strong negative (α_V = -33.67×10^{-6} K^{-1}) to positive by chemical pressure induced by the addition of guest H$_2$O molecules or K$^+$ ions (α_V = 20.3 × 10^{-6} K^{-1} for KYFe(CN)$_6$, α_V = 27.71×10^{-6} K^{-1} for YFe(CN)$_6$·4H$_2$O, α_V= 42.72 ×10^{-6} K^{-1} for KYFe(CN)$_6$·3H$_2$O (Fig. 9b).[14]
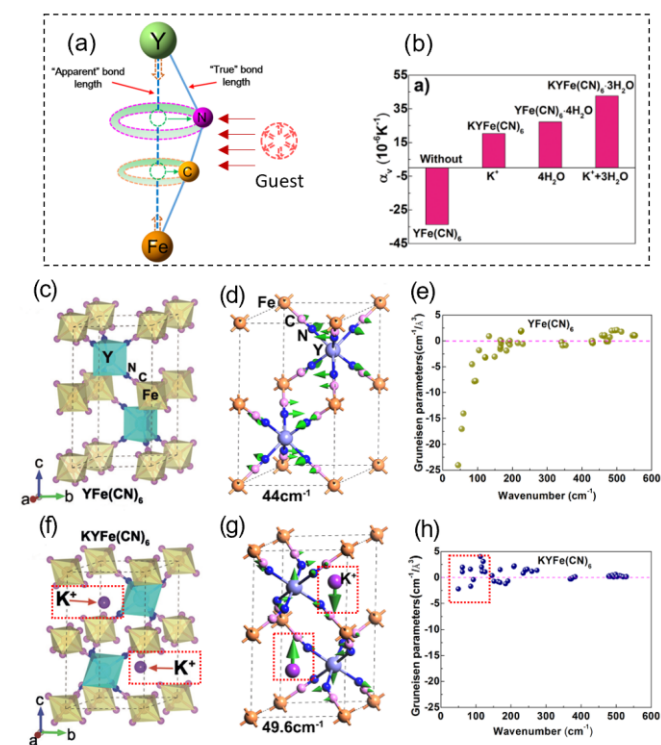
Fig. 9 (a) Schematic presentation of transverse thermal vibration of Y-CN-Fe bond hindered by guest ions or molecules. Due to transverse thermal vibration, the "true" bond lengths are longer than "apparent" bond lengths. (b) A comparison of volumetric coefficient of thermal expansion (α_V) for parent YFe(CN)$_6$ to those with guest K$^+$ ions and H$_2$O molecules. (c-h) Crystal structure (c,f), the main transverse vibrational modes of NTE (d,g), and Grüneisen parameters versus wavenumber for YFe(CN)$_6$ and KYFe(CN)$_6$ (e,h), respectively.

Size effect. Surface atoms have unique electronic states and coordination environments compared with those in the interior. The lattice at the surface of solids usually undergoes a strained state[20]. When particle size decreases to nanoscale, such a lattice strain could penetrate throughout the whole (or most of the) particle. As the size of nanoparticles can be well-controlled by chemical synthesis, we categorize the size effect-induced lattice strain as another type of chemical pressure. Besides lattice strain, the chemical pressure from size effect can even change the structural symmetry, spin state, and phonon vibration when the particle size reduces below a critical value[91, 92].
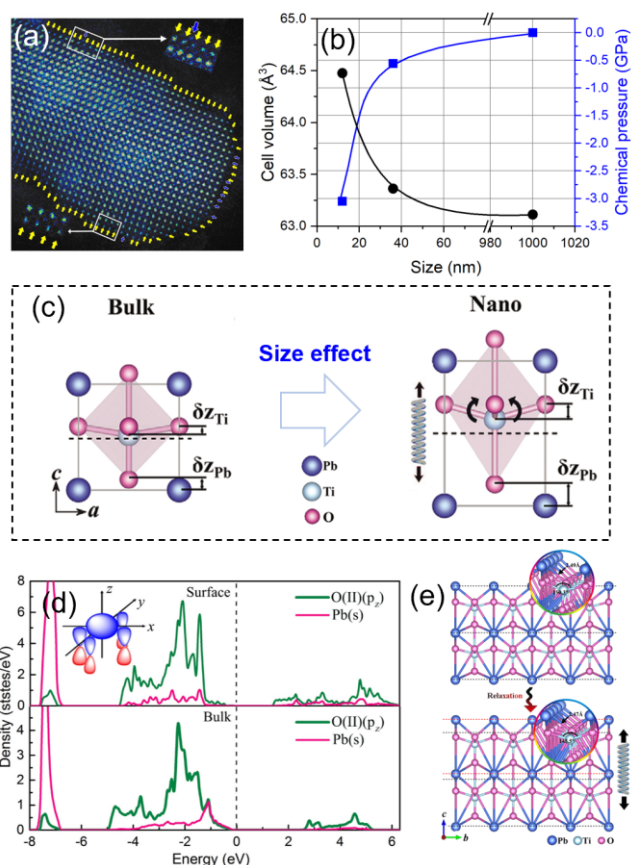
Fig. 10 (a) High-resolution STEM images showing how the PbO-terminal layer dominates PbTiO$_3$ NPs surfaces. (b) Particle size dependence of cell volume and chemical pressure for PbTiO$_3$ NPs. (c) Schematic presentation of size effect-induced structure modification from bulk to nano scale in PbTiO$_3$. (d) Partial density of states of Pb 6s and O 2p_z orbitals of bulk and PbO-terminated surface. Inset shows the geometry configuration of the orbital hybridization. (e) Structural relaxation of the PbO-terminated surface, the inset describes the detailed local structure.

Sun *et al.* synthesized ferroelectric PbTiO$_3$ nanoparticles (NPs) with sizes of 12 nm, 36 nm, and 1 μm through a two-phase solvothermal method[21]. It was found that there exists a negative chemical pressure in PbTiO$_3$ NPs which strengthens with reducing of particle size with $\Delta V/V_{bulk}$ = 0%, 0.4%, and 2.2% for 1 μm (bulk), 36 nm, and 12 nm, corresponding to chemical pressure values of 0 MPa, -558 MPa, and -3.0 GPa (the bulk modulus K of PbTiO$_3$ is 141 GPa[75]), see Fig. 10. The structural origin of the size effect was investigated by X-ray PDF and XAFS analysis. It shows that the nearest Pb-OII bonds (equatorial) shortens with reduced NP size while the nearest Pb-OI bonds (vertex) elongates, accompanied by an enhanced off-centering of Ti ions in the octahedra. Further aberration-corrected STEM images indicate that the as-prepared PbTiO$_3$ NPs surfaces are dominated by PbO-terminal layers. These PbO-terminals are produced by the confined synthesis of the two-phase solvothermal route (Fig. 10b). With particle size decreases to nanoscale, the number of surface ions of nanomaterials increases geometrically: the overall atomic ratio Pb/Ti increases from 1.00 for 1 μm to 1.13 for 12 nm. This significantly alters the average coordination environment of Pb atom and enhances the size effect. Further theoretical calculation shows

that the electronic structure origin of chemical pressure is related to the hybridizations between Pb $6s$ and O $2p_z$ orbitals of PbO-terminated surface and between Ti $3d_z^2$ and O $2p_z$ orbitals of TiO_6 octahedra, which yield raised tetragonality and large spontaneous polarization in $PbTiO_3$ NPs (Fig. 10).[21]

Fig. 11 (a) Temperature dependence of lattice parameters for antiperovskite manganese nitrides $Mn_3Cu_{0.5}Ge_{0.5}N$ with coarse grained, nanocrystalline, and ultrananocrystalline sizes. (b) Magnetic moments of Mn sublattice as a function of temperature for the three materials. The arrows mark the magnetic ordering transition temperatures. Inset shows the magnetic structure of $Mn_3Cu_{0.5}Ge_{0.5}N$.

Antiperovskite manganese nitrides (Mn_3AN, A = Cu, Zn, Sn, etc.) are well-studied for their interesting NTE behaviors driven by magnetism. Song et al. prepared three different microstructures of antiperovskite manganese nitrides $Mn_3Cu_{0.5}Ge_{0.5}N$: coarse-grained polycrystalline (mean grain size ≈ 2.0 μm), nanocrystalline (mean grain size ≈ 30 nm), and ultra-nanocrystalline (mean grain size ≈ 12 nm), see Fig. 11.[93] All these three materials adopt cubic Pm-3m symmetry. Neutron diffraction shows that the Mn occupancy decreases from 100% in the coarse-grained (Mn1000) to ≈ 87.8% in the nanocrystalline (Mn878) and to ≈ 78.7% in the ultra-nanocrystalline (Mn787) material. The cell parameters reduce from 3.91211(9) Å (Mn1000) to 3.89799(7) Å (Mn878) and to 3.89332(7) Å (Mn787). This produces chemical pressures of 0 GPa, 2.7 GPa and 3.6 GPa, respectively. Such size effect weakens the magnetic ordering of Mn sublattice with site 3c Mn moment reducing from ~3.0 μ_B to 2.6 μ_B and 2.2 μ_B, T_C decreasing from 340 K to 260 K and 230 K, for Mn1000, Mn878 and Mn787, respectively. As a result, the CTE changes from strongly negative (α = -17.1× 10^{-6} K^{-1}, 260-340 K) to moderately negative (α = -3.89× 10^{-6} K^{-1}, 160-260 K) and to ZTE (0.118 ×10^{-7} K^{-1}, 12-230 K), see Fig. 11.[93]

Interface constraint. In epitaxial thin films, the lattice of the film is constrained and modulated by the substrate via the "biaxial strain" (binding in-plane but free in the out-of-plane

direction), which is another form of chemical pressure[24, 26, 94]. This method is widely used to favour metastable phases over the equilibrium phase (epitaxial stabilization). Especially for brittle oxides, the lattice strain in the film can reach as large as several %, one order of magnitude larger than that in bulk (~ 0.1%)[94]. As shown in Fig. 12a,12b, through screening substrates with different in-plane lattice constant (changes either substrate type or its orientation), both positive and negative chemical pressure can be achieved, prominently expanding material functions such as ferroelectricity, magnetism, band gap, and superconductivity[22, 24, 48]. When lattice misfit is large, dislocations can arise, which tends to relax the large lattice strain. To avoid these dislocations, the thickness of the film should be below a critical thickness[94, 95].

Xu et al. grew 100 nm α-formamidinium lead iodide (α-$FAPbI_3$) epitaxial films on a series of mixed methylammonium lead chloride/bromide ($MAPbCl_xBr_{3-x}$, 0 ≤ x ≤ 1.5) single crystalline substrates, Fig. 12c,12d[26]. In their freestanding form, both α-$FAPbI_3$ and $MAPbCl_xBr_{3-x}$ are cubic with Pm3m space group. The lattice constants are 6.35 Å for freestanding α-$FAPbI_3$ and 5.83–5.95 Å for $MAPbCl_xBr_{3-x}$ substrates, indicating that a positive in-plane chemical pressure was imposed on the α-$FAPbI_3$ film. As x increases from 0 to 1.5, the lattice parameter a of the substrate reduces, which causes a strain of 2.4% and a biaxial chemical pressure of 1.32 GPa, see Fig. 12e (The chemical pressure is calculated by $P = C_{12} \times \Delta c/c$, where C_{12} is the transverse elastic constant of $FAPbI_3$ (= -5.5±2.2 GPa)[96]). Such a strain effectively changes the crystal structure, reduces the bandgap, increases the hole mobility of α-$FAPbI_3$, and hence increases the external quantum efficiency (Fig. 12f)[26].

Fig. 12 (a) The in-plane lattice misfit between typical substrates and some ferroelectric oxides. (b) Schematic of epitaxially strained thin-film $EuTiO_3$ on the $DyScO_3$ substrate with in-plane negative chemical pressure. (c) Optical images of the epitaxial α-$FAPbI_3$ thin films grown on $MAPbCl_xBr_{3-x}$ substrates. Scale bars, 4 mm. (e) The composition dependence of in-plane chemical pressure of the α-$FAPbI_3$ thin films. Inset is the schematic of lattice misfit. (f) External quantum efficiency spectra of the 1.2% strained and strain-free photodetectors showing that the strained photodetector yields a higher external quantum efficiency as well as a broader absorption spectrum.

Alternative to biaxial strain imposed by 2D substrate, a new interfacial chemical pressure method– "interphase strain" method, was proposed recently[25]. Two materials with similar crystal structures, but different lattice parameters, are used to grow in a single composite with coherent lattice matching. In this way, an isotropic and 3D compression or tensile strain can be introduced into the material that originally had the larger or smaller lattice parameters, respectively. For example, $PbTiO_3$ adopts a tetragonal perovskite structure with lattice constants a = 3.899 Å, c =4.154 Å, and c/a = 1.065 (Fig. 13a); PbO adopts a plate-like tetragonal structure but with a large c/a ratio (a = 3.973 Å, c =5.022 Å, and c/a = 1.264), see Fig. 13b. In the $PbTiO_3$/PbO composite fabricated by "interphase strain" method, $PbTiO_3$ and PbO share the same c lattice constant (4.840 Å) (Fig. 13c-13d). As a result, a super-strong negative chemical pressure of -24 GPa was generated with a super-tetragonal distortion (c/a = 1.238) in $PbTiO_3$ ($\Delta V/V_{bulk}$ = 17.1%), which induces a state-of-art remanent polarization of 236.3 $\mu C/cm^2$ [25].
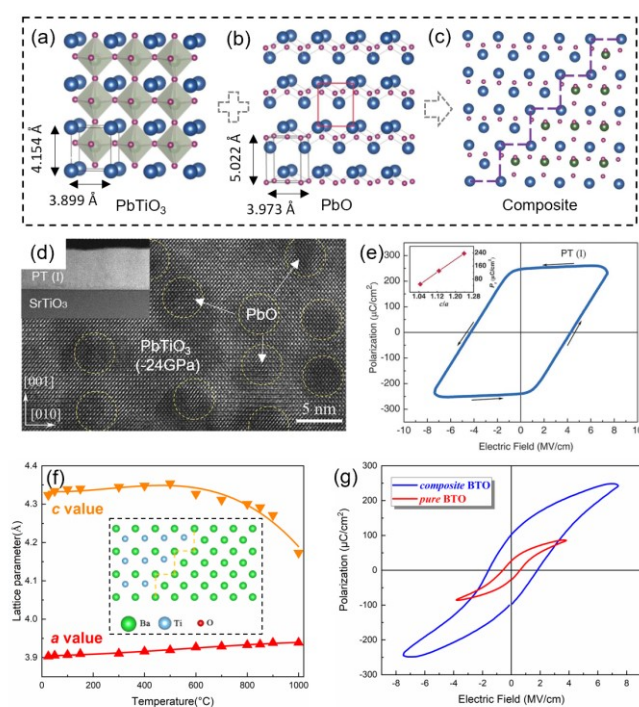

Fig. 13 (a-c) Crystal structure of $PbTiO_3$ (a), PbO (b), and $PbTiO_3$/PbO composite with coherent lattice matching (c). (d) High-resolution STEM image along the a axis of the $PbTiO_3$/PbO composite. The inset displays a low-magnification cross-sectional image. (e) Polarization versus electric field hysteresis loop of the $PbTiO_3$/PbO composite thin films. The inset depicts the remanent polarization as a function of c/a. (f) Temperature dependence of lattice constant of a and c axes for $BaTiO_3$/BaO composite. Inset is the schematics of $BaTiO_3$/BaO interface. (g) ferroelectric hysteresis loops of $BaTiO_3$/BaO composite and pure $BaTiO_3$.

The "interphase strain" method can also be extended to other materials (111).[54] For $BaTiO_3$/BaO, the negative chemical pressure (~ -5.7 GPa) was imposed by the coherent lattice strain from large cubic BaO to small tetragonal $BaTiO_3$, generating high tetragonality (c/a = 1.12) and facilitating large displacements of Ti. This leads to the record remanent polarization P_r (100 $\mu C/cm^2$) in any forms of $BaTiO_3$ to date with

a high Curie temperature T_c (above 1000 °C), see Fig. 13f,13g. It was reported that such negative pressure alters the bonding states, *i.e.* inducing bonding of Ba 5p-O 2p hybridization (which is ionic bonding in bulk), and strong-bonding of Ti e_g and O 2p, which contribute to the tremendously enhanced polarization (111). The interphase strain method has the advantage of providing not only isotropic negative chemical pressure but also isotropic positive chemical pressure, through selective phase matches, and the magnitude of chemical pressure can be modulated by adjusting the composition.[54]

Conclusions and outlook
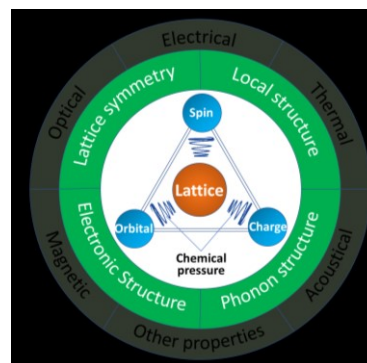
Fig. 14 Schematic presentation of the role of chemical pressure in regulating material structures and their properties.

This review summarizes the development of chemical pressure and defines the concept as a methodology for material design: a lattice internal force caused by chemical modifications. The main feature of chemical pressure is that the lattice strain is caused by a chemical way, instead of physical one, and hence is diverse and does not require extreme conditions. As shown in Fig. 14, applying chemical pressure not only changes the lattice size itself, but can also change the spin, orbital, and charge orderings of the relevant atoms. These changes alter material structures at various levels, including lattice symmetry[53, 97], local structure[8, 9, 82], electronic structure[98, 99], and phonon structure[38, 46], and hence influences material properties by virtue of structure-property relationship (Fig. 14). By proposing two equations for quantification, we can see that the limit of chemical pressure is generally within several GPa, around two orders of magnitude smaller than that of the highest achievable physical pressures. The largest value, -24 GPa to our best knowledge, was realized via a newly proposed "interphase strain" method in a $PbTiO_3$/PbO coherent lattice, and is accompanied by an unusual ferroelectric response[25]. More novel methods enabling stronger chemical pressures would be highly attractive to realize striking or unusual properties in the future. More details, such as local strain gradient and its propagation from substitution site, and the electronic and phonon structures induced by the breaking of ideal 3D translational periodicity, remain for further exploration of new phenomena in solids by chemical pressure methods.

Conflicts of interest

Acknowledgements

Notes and references

1. T. W. Richards, *Trans. Faraday Soc.*, 1928, **24**, 111-120.
2. T. W. Richards, *Chem. Rev.*, 1925, **2**, 315-348.
3. I. Nowik, I. Felner, Voiron, Beille, Najib, E. du Tremolet de Lacheisserie and Gratz, *Phys. Rev. B*, 1988, **37**, 5633-5638.
4. W. Kleber, *Kristall und Technik*, 1967, **2**, 13-14.
5. J. G. Bednorz and K. A. Mller, *Z. Phys., B Condens. Matter.*, 1986, **64**, 189-193.
6. Y. Kamihara, T. Watanabe, M. Hirano and H. Hosono, *J. Am. Chem. Soc.*, 2008, **130**, 3296-3297.
7. M. K. Wu, J. R. Ashburn, C. J. Torng, P. H. Hor, R. L. Meng, L. Gao, Z. J. Huang, Y. Q. Wang and C. W. Chu, *Phys. Rev. Lett.*, 1987, **58**, 908-910.
8. L. Hu, J. Chen, L. Fan, Y. Ren, Y. Rong, Z. Pan, J. Deng, R. Yu and X. Xing, *J. Am. Chem. Soc.*, 2014, **136**, 13566-13569.
9. D. C. Fredrickson, *Acc. Chem. Res.*, 2018, **51**, 248-257.
10. F. Li, M. J. Cabral, B. Xu, Z. Cheng, E. C. Dickey, J. M. LeBeau, J. Wang, J. Luo, S. Taylor, W. Hackenberger, L. Bellaiche, Z. Xu, L. Q. Chen, T. R. Shrout and S. Zhang, *Science*, 2019, **364**, 264-268.
11. P. L. Wang, T. Kolodiazhnyi, J. Yao and Y. Mozharivskyj, *J. Am. Chem. Soc.*, 2012, **134**, 1426-1429.
12. B. Qin, D. Wang, W. He, Y. Zhang, H. Wu, S. J. Pennycook and L. D. Zhao, *J. Am. Chem. Soc.*, 2019, **141**, 1141-1149.
13. J. Chen, Q. Gao, A. Sanson, X. Jiang, Q. Huang, A. Carnera, C. G. Rodriguez, L. Olivi, L. Wang, L. Hu, K. Lin, Y. Ren, Z. Lin, C. Wang, L. Gu, J. Deng, J. P. Attfield and X. Xing, *Nat. Commun.*, 2017, **8**, 14441.
14. Q. Gao, J. Chen, Q. Sun, D. Chang, Q. Huang, H. Wu, A. Sanson, R. Milazzo, H. Zhu, Q. Li, Z. Liu, J. Deng and X. Xing, *Ang. Chem. Int. Ed.,* 2017, **56**, 9023-9028.
15. M. Nakaya, W. Kosaka, H. Miyasaka, Y. Komatsumaru, S. Kawaguchi, K. Sugimoto, Y. Zhang, M. Nakamura, L. F. Lindoy and S. Hayami, *Ang. Chem. Int. Ed.,* 2020, **59**, 10658-10665.
16. J. Zhang, W. Kosaka, Y. Kitagawa and H. Miyasaka, *Nat Chem*, 2021, **13**, 191-199.
17. X. G. Zheng, H. Kubozono, H. Yamada, K. Kato, Y. Ishiwata and C. N. Xu, *Nat. Nanotechnol.*, 2008, **3**, 724-726.
18. J. Wang, B. Wylie-van Eerd, T. Sluka, C. Sandu, M. Cantoni, X. K. Wei, A. Kvasov, L. J. McGilly, P. Gemeiner, B. Dkhil, A. Tagantsev, J. Trodahl and N. Setter, *Nat. Mater.*, 2015, **14**, 985-990.
19. Q. Li, H. Zhu, L. Zheng, L. Fan, Y. Ren, J. Chen, J. Deng and X. Xing, *Adv. Sci.*, 2016, **3**, 1600108.
20. Q. Li, H. Zhu, L. Hu, J. Chen and X. Xing, *Acc. Chem. Res.*, 2019, **52**, 2694-2702.
21. J. Sun, Q. Li, H. Zhu, Z. Liu, K. Lin, N. Wang, Q. Zhang, L. Gu, J. Deng, J. Chen and X. Xing, *Adv. Mater.*, 2020, **32**, e2002968.
22. J. H. Lee, L. Fang, E. Vlahos, X. Ke, Y. W. Jung, L. F. Kourkoutis, J.-W. Kim, P. J. Ryan, T. Heeg, M. Roeckerath, V. Goian, M. Bernhagen, R. Uecker, P. C. Hammel, K. M. Rabe, S. Kamba, J. Schubert, J. W. Freeland, D. A. Muller, C. J. Fennie, P. Schiffer, V. Gopalan, E. Johnston-Halperin and D. G. Schlom, *Nature*, 2010, **466**, 954-958.
23. J. S. White, M. Bator, Y. Hu, H. Luetkens, J. Stahn, S. Capelli, S. Das, M. Dobeli, T. Lippert, V. K. Malik, J. Martynczuk, A. Wokaun, M. Kenzelmann, C. Niedermayer and C. W. Schneider, *Phys. Rev. Lett.*, 2013, **111**, 037201.
24. A. K. Yadav, C. T. Nelson, S. L. Hsu, Z. Hong, J. D. Clarkson, C. M. Schlepuetz, A. R. Damodaran, P. Shafer, E. Arenholz, L. R. Dedon, D. Chen, A. Vishwanath, A. M. Minor, L. Q. Chen, J. F. Scott, L. W. Martin and R. Ramesh, *Nature*, 2016, **530**, 198-201.
25. L. Zhang, J. Chen, L. Fan, O. Dieguez, J. Cao, Z. Pan, Y. Wang, J. Wang, M. Kim, S. Deng, J. Wang, H. Wang, J. Deng, R. Yu, J. F. Scott and X. Xing, *Science*, 2018, **361**, 494-497.
26. Y. Chen, Y. Lei, Y. Li, Y. Yu, J. Cai, M. H. Chiu, R. Rao, Y. Gu, C. Wang, W. Choi, H. Hu, C. Wang, Y. Li, J. Song, J. Zhang, B. Qi, M. Lin, Z. Zhang, A. E. Islam, B. Maruyama, S. Dayeh, L. J. Li, K. Yang, Y. H. Lo and S. Xu, *Nature*, 2020, **577**, 209-215.
27. P. F. McMillan, *Nat. Mater.*, 2005, **4**, 715-718.
28. M. Miao, Y. Sun, E. Zurek and H. Lin, *Nat. Rev. Chem.*, 2020, **4**, 508-527.
29. A. Lazicki, D. McGonegle, J. R. Rygg, D. G. Braun, D. C. Swift, M. G. Gorman, R. F. Smith, P. G. Heighway, A. Higginbotham, M. J. Suggit, D. E. Fratanduono, F. Coppari, C. E. Wehrenberg, R. G. Kraus, D. Erskine, J. V. Bernier, J. M. McNaney, R. E. Rudd, G. W. Collins, J. H. Eggert and J. S. Wark, *Nature*, 2021, **589**, 532-535.
30. J.-M. Fournier, *Phys. B Condens. Matter.*, 1993, **190**, 50-54.
31. Y. Kamihara, T. Watanabe, M. Hirano and H. Hosono, *J. Am. Chem. Soc.*, 2008, **130**, 3296-3297.
32. W. L. McMillan, *Phys. Rev.*, 1968, **167**, 331-344.
33. H. Takahashi, K. Igawa, K. Arii, Y. Kamihara, M. Hirano and H. Hosono, *Nature*, 2008, **453**, 376-378.
34. G. R. Stewart, *Rev. Mod. Phys.* 2011, **83**, 1589-1652.
35. J. A. Rodgers, G. B. S. Penny, A. Marcinkova, J.-W. G. Bos, D. A. Sokolov, A. Kusmartseva, A. D. Huxley and J. P. Attfield, *Phys. Rev. B*, 2009, **80**.
36. K. Kuroki, H. Usui, S. Onari, R. Arita and H. Aoki, *Phys. Rev. B*, 2009, **79**.
37. Y. Mizuguchi, Y. Hara, K. Deguchi, S. Tsuda, T. Yamaguchi, K. Takeda, H. Kotegawa, H. Tou and Y. Takano, *Supercond. Sci. Technol.*, 2010, **23**.
38. V. D'Anna, L. M. L. Daku, H. Hagemann and F. Kubel, *Phys. Rev. B*, 2010, **82**.
39. Z. Wu and R. E. Cohen, *Phys. Rev. Lett.*, 2005, **95**, 037601.
40. A. Kvasov, L. J. McGilly, J. Wang, Z. Shi, C. S. Sandu, T. Sluka, A. K. Tagantsev and N. Setter, *Nat. Commun.*, 2016, **7**, 12136.
41. X. T. Li, Y. P. Fu, L. Pedesseau, P. J. Guo, S. Cuthriell, I. Hadar, J. Even, C. Katan, C. C. Stoumpos, R. D. Schaller, E. Harel and M. G. Kanatzidis, *J. Am. Chem. Soc.*, 2020, **142**, 11486-11496.
42. Fernandes, Santamaria, Bud'ko, Nakamura, Guimpel and Schuller, *Phys. Rev. B*, 1991, **44**, 7601-7606.
43. L. E. Klintberg, S. K. Goh, S. Kasahara, Y. Nakai, K. Ishida, M. Sutherland, T. Shibauchi, Y. Matsuda and T. Terashima, *J. Phys. Soc. Jpn.*, 2010, **79**, 123706.
44. T. Tiittanen and M. Karppinen, *J. Solid State Chem.*, 2017, **246**, 245-251.
45. K. K. Gopinathan and A. R. K. L. Padmini, 1975, **16**, 817.
46. L. Hu, F. Qin, A. Sanson, L.-F. Huang, Z. Pan, Q. Li, Q. Sun, L. Wang, F. Guo, U. Aydemir, Y. Ren, C. Sun, J. Deng, G. Aquilanti, J. M. Rondinelli, J. Chen and X. Xing, *J. Am. Chem. Soc.*, 2018, **140**, 4477-4480.
47. R. B. Wexler, J. M. P. Martirez and A. M. Rappe, *J. Am. Chem. Soc.*, 2018, **140**, 4678-4683.
48. N. M. Dawley, E. J. Marksz, A. M. Hagerstrom, G. H. Olsen, M. E. Holtz, V. Goian, C. Kadlec, J. Zhang, X. Lu, J. A. Drisko, R. Uecker, S. Ganschow, C. J. Long, J. C. Booth, S. Kamba, C. J.

Fennie, D. A. Muller, N. D. Orloff and D. G. Schlom, *Nat. Mater.*, 2020, **19**, 176-181.

49. L. Zhang, D. Zheng, L. Fan, J. Wang, M. Kim, J. Wang, H. Wang, X. Xing, J. Tian and J. Chen, *Nano Lett*, 2020, **20**, 881-886.
50. D. C. Fredrickson, *J. Am. Chem. Soc.*, 2011, **133**, 10070-10073.
51. D. C. Fredrickson, *J. Am. Chem. Soc.*, 2012, **134**, 5991-5999.
52. S. Lee, *Ann. Rev. Phys. Chem.*, 1996, **47**, 397-419.
53. B. J. Kilduff and D. C. Fredrickson, *Inorganic Chemistry*, 2016, **55**, 6781-6793.
54. Y. Wang, L. Zhang, J. Wang, Q. Li, H. Wang, L. Gu, J. Chen, J. Deng, K. Lin, L. Huang and X. Xing, *J. Am. Chem. Soc.*, 2021, **143**, 6491-6497.
55. J. H. Westbrook and R. L. Fleischer, *Basic Mechanical Properties and Lattice Defects of Intermetallic Compounds*, Wiley. R. L., 2000.
56. E. G. Moloney, V. Yeddu and M. I. Saidaminov, *ACS Mater. Lett.*, 2020, **2**, 1495-1508.
57. L. Gerward, J. Staun Olsen, L. Petit, G. Vaitheeswaran, V. Kanchana and A. Svane, *J. Alloys Compt.*, 2005, **400**, 56-61.
58. J. R. McBride, K. C. Hass, B. D. Poindexter and W. H. Weber, *J. Appl. Phys.*, 1994, **76**, 2435-2441.
59. P. Kulandaivelu, K. Sakthipandi, P. Senthil Kumar and V. Rajendran, *J. Phys. Chem. Solid.*, 2013, **74**, 205–214.
60. J. Hemberger, A. Krimmel, T. Kurz, K. V. N. H.-A., V. Y. Ivanov, A. A. Mukhin, A. M. Balbashov and A. Loidl, *Phys. Rev. B*, 2002, **66**, 094410.
61. A., J. and Millis, *Nature*, 1998, **392**, 147–150.
62. S. Margadonna, Y. Takabayashi, Y. Ohishi, Y. Mizuguchi, Y. Takano, T. Kagayama, T. Nakagawa, M. Takata, Prassides and K., *Phys. Rev. B*, 2009, **80**, 1956-1960.
63. F.-C. Hsu, J.-Y. Luo, K.-W. Yeh, T.-K. Chen, T.-W. Huang, P. M. Wu, Y.-C. Lee, Y.-L. Huang, Y.-Y. Chu, D.-C. Yan and M.-K. Wu, *Proc. Natl. Acad. Sci.*, 2008, **105**, 14262-14264.
64. A. Bentouaf, R. Mebsout, H. Rached, S. Amari, A. H. Reshak and B. Aissa, *J. Alloys Compt.*, 2016, **689**, 885-893.
65. Y. Song, J. Chen, X. Liu, C. Wang, J. Zhang, H. Liu, H. Zhu, L. Hu, K. Lin and S. Zhang, *J. Am. Chem. Soc.*, 2018, **140**, 602-605.
66. A. Fantin, G. O. Lepore, A. M. Manzoni, S. Kasatikov, T. Scherb, T. Huthwelker, F. d'Acapito and G. Schumacher, *Acta. Mater.*, 2020, **193**, 329-337.
67. S. S. Sohn, A. Kwiatkowski da Silva, Y. Ikeda, F. Körmann, W. Lu, W. S. Choi, B. Gault, D. Ponge, J. Neugebauer and D. Raabe, *Adv. Mater.*, 2019, **31**, 1807142.
68. S. Ganeshan, S. L. Shang, Y. Wang and Z. K. Liu, *Acta. Mater.*, 2009, **57**, 3876-3884.
69. F. W. V. Batchelder and R. F. Raeuchle, *Phys. Rev.*, 1957, **105**, 59-61.
70. H. Zhu, C. Yang, Q. Li, Y. Ren, J. C. Neuefeind, L. Gu, H. Liu, L. Fan, J. Chen, J. Deng, N. Wang, J. Hong and X. Xing, *Nat. Commun.*, 2018, **9**, 5063.
71. V. Swamy, L. S. Dubrovinsky, N. A. Dubrovinskaia, A. S. Simionovici, M. Drakopoulos, V. Dmitriev and H.-P. Weber, *Solid State Commun.*, 2003, **125**, 111-115.
72. H. Zhu, Q. Li, Y. Ren, L. Fan, J. Chen, J. Deng and X. Xing, *Adv. Mater.*, 2016, **28**, 6894-6899.
73. G. A. Zvyagina, T. N. Gaydamak, K. R. Zhekov, I. V. Bilich, V. D. Fil, D. A. Chareev and A. N. Vasiliev, *EPL*, 2013, **101**, 56005.
74. S. Tan, Y. Zhang, M. Xia, Z. Ye, F. Chen, X. Xie, R. Peng, D. Xu, Q. Fan, H. Xu, J. Jiang, T. Zhang, X. Lai, T. Xiang, J. Hu, B. Xie and D. Feng, *Nat. Mater.*, 2013, **12**, 634-640.
75. S. Piskunov, E. Heifets, R. I. Eglitis and G. Borstel, *Compt. Mater. Sci.*, 2004, **29**, 165-178.
76. L. J. Z. F. P. Vegard, 1921, **5**, 17-26.
77. R. Mittal, M. K. Gupta and S. L. Chaplot, *Prog. Mater. Sci.*, 2018, **92**, 360-445.
78. A. P. Ramirez, G. Ernst, C. Broholm and G. R. Kowach, *Nature*, 1998, **396**, 147-149.
79. B. K. Greve, K. L. Martin, P. L. Lee, P. J. Chupas, K. W. Chapman and A. P. Wilkinson, *J. Am. Chem. Soc.*, 2010, **132**, 15496-15498.
80. C. W. Li, X. Tang, J. A. Muñoz, J. B. Keith, S. J. Tracy, D. L. Abernathy and B. Fultz, *Phys. Rev. Lett.*, 2011, **107**, 195504.
81. Q. Gao, J. Wang, A. Sanson, Q. Sun, E. Liang, X. Xing and J. Chen, *J. Am. Chem. Soc.*, 2020, **142**, 6935-6939.
82. L. Hu, J. Chen, J. Xu, N. Wang, F. Han, Y. Ren, Z. Pan, Y. Rong, R. Huang, J. Deng, L. Li and X. Xing, *J. Am. Chem. Soc.*, 2016, **138**, 14530-14533.
83. F. Li, D. Lin, Z. Chen, Z. Cheng, J. Wang, C. Li, Z. Xu, Q. Huang, X. Liao, L. Q. Chen, T. R. Shrout and S. Zhang, *Nat. Mater.*, 2018, **17**, 349-354.
84. B. Narayan, J. S. Malhotra, R. Pandey, K. Yaddanapudi, P. Nukala, B. Dkhil, A. Senyshyn and R. Ranjan, *Nat. Mater.*, 2018, **17**, 427-431.
85. V. M. Goldschmidt, *Naturwissenschaften*, 1926, **14**, 477-485.
86. S. Vasala and M. Karppinen, *Prog. Solid Stat. Chem.*, 2015, **43**, 1-36.
87. J. P. Attfield, *Int. J. Inorg. Mater.*, 2001, **3**, 1147-1152.
88. C. Q. Jin, J. S. Zhou, J. B. Goodenough, Q. Q. Liu, J. G. Zhao, L. X. Yang, Y. Yu, R. C. Yu, T. Katsura, A. Shatskiy and E. Ito, *Proc. Natl. Acad. Sci. U. S. A.*, 2008, **105**, 7115-7119.
89. S. Nishikiori, H. Yoshikawa, Y. Sano and T. Iwamoto, *Acc. Chem. Res.*, 2005, **38**, 227-234.
90. P. D. Southon, L. Liu, E. A. Fellows, D. J. Price, G. J. Halder, K. W. Chapman, B. Moubaraki, K. S. Murray, J.-F. Létard and C. J. Kepert, *J. Am. Chem. Soc.*, 2009, **131**, 10998-11009.
91. Y. W. Jun, J. W. Seo and J. Cheon, *Acc. Chem. Res.*, 2008, **41**, 179-189.
92. H. Zhu, C. Yang, Q. Li, Y. Ren, J. C. Neuefeind, L. Gu, H. Liu, L. Fan, J. Chen, J. Deng, N. Wang, J. Hong and X. Xing, *Nat. Commun.*, 2018, **9**, 5063.
93. X. Song, Z. Sun, Q. Huang, M. Rettenmayr, X. Liu, M. Seyring, G. Li, G. Rao and F. Yin, *Adv. Mater.*, 2011, **23**, 4690-4694.
94. D. G. Schlom, L.-Q. Chen, C. J. Fennie, V. Gopalan, D. A. Muller, X. Pan, R. Ramesh and R. Uecker, *MRS Bull.*, 2014, **39**, 118-130.
95. M. D. Biegalski, D. D. Fong, J. A. Eastman, P. H. Fuoss, S. K. Streiffer, T. Heeg, J. Schubert, W. Tian, C. T. Nelson, X. Q. Pan, M. E. Hawley, M. Bernhagen, P. Reiche, R. Uecker, S. Trolier-McKinstry and D. G. Schlom, *J. Appl. Phys.*, 2008, **104**, 114109.
96. A. C. Ferreira, A. Letoublon, S. Paofai, S. Raymond, C. Ecolivet, B. Ruffle, S. Cordier, C. Katan, M. I. Saidaminov, A. A. Zhumekenov, O. M. Bakr, J. Even and P. Bourges, *Phys. Rev. Lett.*, 2018, **121**, 085502.
97. Y. Han, C. Zhu, Y. Peng, S. Li, M. Wu, S. Zhao, Z. Deng, C. Jin, W. Du, D. Walker and M.-R. Li, *Chem. Mater.*, 2020, **32**, 1618-1626.
98. X. Tan, G. Fabbris, D. Haskel, A. A. Yaroslavtsev, H. Cao, C. M. Thompson, K. Kovnir, A. P. Menushenkov, R. V. Chernikov, V. O. Garlea and M. Shatruk, *J. Am. Chem. Soc.*, 2016, **138**, 2724-2731.
99. D. D. Khalyavin, R. D. Johnson, F. Orlandi, P. G. Radaelli, P. Manuel and A. A. Belik, *Science*, 2020, **369**, 680-684.